Band-structure approach to the x-ray spectra of metals

Jorge E. Müller
Institut für Festkörperforschung der Kernforschungsanlage Jülich, D-5170 Jülich, West Germany

John W. Wilkins
Laboratory of Atomic and Solid State Physics and the Materials Science Center, Cornell University, Ithaca, New York 14853

(Received 15 August 1983)

A formalism to compute x-ray spectra due to core excitations in metals by using single-particle band-structure techniques is presented and illustrated with a detailed calculation of the K, L, and M emission and absorption spectra of palladium over 200 eV. Within the muffin-tin approximation for the potential, any spectrum can be factorized into atomiclike and solid-state contributions. The atomiclike factor is the dipole transition strength connecting a core state to a muffin-tin orbital in a free-electron metal. The solid-state factor is proportional to the density of band states with angular momentum determined by the orbital symmetry of the core state and the dipole selection rules. These projected densities of states have been calculated by using a linearized version of the augmented-plane-wave method specifically designed to cover large energy ranges. In particular, the method can describe simultaneously several principal quantum numbers of the eigenstates (e.g., $4d$ and $5d$ for palladium).

I. INTRODUCTION

The emission and absorption of x rays are among the most simple probes of the occupied and unoccupied electron states in solids.[1] Historically, the first measure of the width of a partially filled conduction band came from x-ray emission. Today synchrotron-radiation facilities make x-ray absorption an attractive experimental tool: Good-quality, highly resolved, absolute measurements can readily be obtained. All core states are now accessible (from 35 eV for the sodium L edge to 100 keV for the uranium K edge), and there is sufficient intensity to measure the spectrum far above the edge.

The procedures employed so far to compute x-ray-absorption spectra have been based on one of two approaches: the scattering formalism (short range) or band-structure calculations (long range). The simplest short-range approach is represented by the standard extended x-ray-absorption fine-structure (EXAFS) formula, which has been extensively applied to interpret EXAFS's.[2] This formula fully includes the effect of the central atom, but treats that of the neighboring atoms only via single back-scattering events, and is therefore restricted to energies far above threshold where the atomic cross sections become smaller. Recently, the short-range approach was extended to low energies by including multiple scattering events[3] and it was successfully applied to compute a variety of near-edge structures. On the other hand, reported calculations of absorption spectra using conventional band-structure methods have been restricted to the near-edge region.

Using the augmented-plane-wave (APW) method, Szmulowicz *et al.* calculated the K-edge spectrum of Al (Ref. 4) up to 23 eV above the Fermi level and the K and L edges of Ni (Ref. 5) up to 41 eV above the Fermi level, and identified the symmetry levels associated with each feature of the spectrum. In order to discuss the relative importance of band-structure and many-body effects at threshold, Gupta *et al.* calculated the K edge of Li (Ref. 6) and the $L_{2,3}$ edge of Na (Ref. 7) and Mg (Ref. 8) up to 2 or 3 eV above the Fermi level. Papaconstantopoulos and co-workers calculated the K edge of Ca (Ref. 9) and the L edge of Ni (Ref. 10) up to 17 eV above the Fermi level and both the Ti and Fe K edges of TiFe (Ref. 11) up to 10 eV above the Fermi level. Wakoh and Kubo[12] calculated the K edges of V, Fe, Ni, and Cu up to 30 eV above the Fermi level. In prevous work[13] in the present research program, the K edges of Zr, Mo, Pd, and Ag have been calculated up to 60 eV above the Fermi level using Andersen's linear APW method,[14] and the systematic trend of the main features of the spectra along the $4d$ row has been discussed. In this paper a formalism for calculating x-ray spectra due to core excitations in metals over an extended energy range based on a more suitable band-structure method is presented and illustrated with a detailed calculation of the palladium K-, L-, and M-edge spectra up to 200 eV above threshold. An extensive application of the scheme to the K edges of $3d$ metals and the L edges of $3d$ and $4d$ metals has been presented elsewhere.[15]

A principal result of this work is that the spectra can be understood as the product of an atomiclike term and a solid-state term. This factorization results from the localized nature of the core state involved in the x-ray transition. Further, since the dipole transition dominates the process, excitation of a core state having orbital angular momentum l probes the $l\pm1$ components of the conduction band. The $l-1$ term exhibits a much smaller transition amplitude and can be ignored in the discussion (although it is included in our calulation). We are thus lead to the following simple understanding of the x-ray spectra: (1) The overall magnitude and shape of a particular spectrum is determined by the corresponding atomic tran-

sition rate, and (2) the fine structure of the spectrum is determined by a solid-state factor which is proportional to the density of band states with $l+1$ orbital character. Thus, using core states with different orbital symmetry, one can study the angular momentum content of the band states, the states below (above) the Fermi level showing up in the emission (absorption) part of the spectrum.

The calculation of the absorption part of the spectrum using a band-structure approach requires the knowledge of conduction-band energies and wave functions to quite high energies. This adds to the magnitude and complexity of the calculation because of the large number of energy levels in the high-energy region of the spectrum. For each Bloch vector $\vec{k}$ the number of levels up to a given $E_{\max}$ (in Ry) is given roughly by $N=\Omega(E_{\max}^{3/2}/3\pi^2)$, where Ω is the volume of the primitive cell in atomic units. In the case of palladium, with $\Omega=99.4a_0^3$, up to $E_{\max}=10$ Ry, there are $N\sim 107$ energy levels for each Bloch vector. Moreover, at least 256 Bloch vectors in the irreducible part ($\frac{1}{48}$th wedge for cubic systems) of the Brillouin zone are required to accurately evaluate the $\vec{k}$ sums at high energies. In order to solve the band-structure problem, we have used a modification[16] of the linear-APW method of Andersen.[14] The main difference is that in the new scheme, computed logarithmic derivative functions themselves are used, instead of a parametrization of them, and as a result, an arbitrary range of principal quantum numbers of the energy eigenstates can be handled simultaneously. It is this feature which makes the scheme uniquely suited to the calculation of absorption spectra.

The central approximation of our formalism is that x-ray absorption and emission are treated as single-particle processes. This necessarily means that we cannot calculate the singularities near the edge.[17] Nonetheless, such a single-particle calculation is a necessary first step in the understanding of the x-ray spectra and their systematic trends in the Periodic Table. Furthermore, deviations of the experiments from accurate single-particle calculations may point the way to many-body effects. One such effect involves the filling of the core hole and the decay of the electron excited in the absorption. This effect has been phenomenologically incorporated in the present calculation by convoluting the single-particle result with a Lorentzian broadening function whose width is equal to the sum of the inverse lifetimes of the core hole and the excited electron.

The potential employed in this calculation was constructed from a superposition of atomic charge densities. This potential, even though it may not reproduce all the detailed features of the occupied states, is quite adequate for describing the higher-energy states. These states are mostly affected by the part of the potential close to the nuclei, where it is essentially equal to the atomic potential. Use of a self-consistent potential leaves all high-energy features unaffected; the $4d$ band, however, moves about 1 eV higher in energy, producing minor changes in the absorption spectra, which extend up to about 8 eV above threshold. Consistent with our band-structure approach, we use a strictly periodic potential. This is appropriate for the x-ray-emission problem, while for the x-ray-absorption problem it might be preferable to use a potential with a core hole. It has been suggested that the localized core-hole potential may give rise to energy shifts in the placement of the high-energy features of the spectra.[18] In the present calculation, we have used self-consistent Dirac core wave functions and have computed the band states including all scalar relativity corrections. The inclusion of spin-orbit coupling in the band states is expected to have a negligible effect for all but the heaviest elements ($Z\gtrsim 75$); it will be discussed elsewhere.

Finally, it should be pointed out that the high-energy bands and wave functions could be employed for a number of other uses besides x-ray spectra. Some of the experimental techniques which also probe high-energy levels are angle-resolved x-ray-photoemission spectroscopy, bremsstrahlung isochromat spectroscopy, electron-energy-loss spectroscopy, and photoelectric yield spectroscopy.

In Sec. II we describe our approach to analyzing x-ray spectra as a product of atomiclike and solid-state factors; the detailed derivations can be found in Appendixes B and C. In Sec. III we present our linearized version of the APW method. Practical aspects of the scheme are discussed in Sec. IV in terms of an application to palladium. Finally, in Sec. V the physical origin of the relevant features of the spectra is discussed. Unless otherwise stated, we use atomic Rydberg units, which we have summarized in Appendix A.

II. X-RAY SPECTRUM

Both the x-ray absorption and emission spectra of a core level $c=(n,l,J)$ with energy E_c and wave functions ϕ_{cM} are proportional to the spectral distribution $F_c(E)$ of the oscillator strength, given by[19,20]

$$F_c(E)=\frac{\omega}{3}\sum_{\vec{k},j}\sum_{M=-J}^{J} r^2_{cM,\vec{k}j}\,\delta(E-E_{\vec{k}j}) , \tag{2.1}$$

where

$$\vec{r}_{cM,\vec{k}j}=\langle \phi_{cM}\vec{r}\psi_{\vec{k}j}\rangle . \tag{2.2}$$

Here $E_{\vec{k}j}$ and $\psi_{\vec{k}j}$ are the energy and wave function of the jth conduction band at reduced vector $\vec{k}$, $\omega=E-E_c$ is the energy of the emitted or absorbed photon, and $\langle\ \rangle=\int d^3r(\ )$ denotes integration over the volume Ω of the primitive cell. The contribution μ_c of the cth core level to the absorption coefficient μ (in units of bohr^{-1}) can be expressed as[16]

$$\mu_c(E)=\frac{4\pi^2\alpha}{\Omega/\nu}F_c(E) , \quad E>E_F \tag{2.3}$$

where $\alpha^{-1}=137.036$ is the inverse fine-structure constant, E_F is the Fermi energy, and ν is the number of contributing atoms in the primitive cell. The corresponding emission intensity I_c for a hole created in the cth core shell is given by[16]

$$I_c(E)=(\alpha\omega)^3F_c(E), \quad E<E_F . \tag{2.4}$$

In deriving the previous expressions, we have introduced the following limitations. (i) We have averaged over the polarization $\hat{\epsilon}_{\vec{q}}$ and the direction of the wave

vector $\vec{q}$ of the photon in order to describe polycrystalline samples. If needed, the fully anisotropic expression can be recovered by replacing $r^2_{cM,\vec{k}j}$ by $3\,|\,\hat{e}_{\vec{q}}\cdot\vec{r}_{cM,\vec{k}j}\,|^2$ in (2.1). (ii) We have employed the electric-dipole approximation, which neglects the spatial variation $e^{i\vec{q}\cdot\vec{r}}$ of the electric field of the x rays over the region where the core wave function is appreciable. As the energy of the x rays increases, this approximation becomes less reliable and one may need to include further tems. In Table I, we show the ratio of the electric-quadrupole to the electric-dipole contributions, and we observe that the neglect of quadrupole terms is justified for systems of lower atomic number.

For completeness we rewrite the experimental quantities (2.1), (2.3), and (2.4) in cgs units as

$$F_c(E)=\frac{2m}{3\hbar^2}(\hbar\omega)\sum_{\vec{k}j}\sum_{M}|\langle\phi_{cM}|\vec{r}|\psi_{\vec{k}j}\rangle|^2\delta(E-E_{\vec{k}j})\,, \tag{2.1'}$$

$$\mu_c(E)=\frac{2\pi^2e^2\hbar}{mc}\frac{\nu}{\Omega}F_c(E),\quad E>E_F \tag{2.3'}$$

$$I_c(E)=\frac{2e^2\hbar\omega^3}{mc^3}F_c(E),\quad E<E_F\,. \tag{2.4'}$$

A. Spectral distribution of the oscillator strength

Here we construct an angular momentum decomposition of the oscillator strength which is consistent with the band-structure approach and allows an identification of atomiclike and solid-state effects in the spectra. This decomposition, which is the same that is used in the scattering formalism, will permit us to make the connection between both theories and will prove useful in discussing the results. In Appendix B we show that, with the neglect of spin-orbit coupling for the band states, the spectral distribution of oscillator strength F_c for a core state $c=(n,l,J)$ can be written as[21]

$$F_c=\frac{\omega}{3}\frac{2J+1}{2(2l+1)}\left[\frac{l}{2l-1}f_{c,l-1}(E)+\frac{l+1}{2l+1}f_{c,l+1}(E)\right] \tag{2.5}$$

where ω is the energy of the x rays, and

TABLE I. Validity of the electric-dipole approximation. The average value of the ratio $\langle c\,|\,q^2r^2\,|\,\vec{k},j\rangle^2/\langle c\,|\,qr\,|\,\vec{k},j\rangle^2$ of the electric-quadrupole to electric-dipole contributions over states $|\,\vec{k},j\rangle$ up to 3 Ry above E_F is given for various systems and different core levels $|\,c\rangle$. We expect the electric-dipole approximation to be satisfactory for the systems above the dashed lines.

Element	K (1s)	L_1 (2s)	$L_{2,3}$ (2p)
$_{13}$Al	0.012	0.004	0.001
$_{29}$Cu	0.058	0.026	0.010
$_{47}$Ag	0.152	0.073	0.029
$_{70}$Yb	0.314	0.194	0.063
$_{79}$Au	0.397	0.270	0.084

$$f_{c,l}(E)=\frac{\langle\phi_c\vec{r}\phi_l(E)\rangle^2}{\langle\phi_l^2(E)\rangle}N_l(E)\,. \tag{2.6}$$

The angular-momentum-projected density of states N_l is defined as

$$N_l(E)=2\sum_{\vec{k},j}\sum_{m}|\langle Y_{lm}|\psi_{\vec{k}j}\rangle|^2\delta(E-E_{\vec{k}j})\,. \tag{2.7}$$

The wave function $\phi_l(E,r)$ is a solution of the radial Schrödinger equation inside the muffin-tin (MT) sphere of radius $S=S_{\rm MT}$, and is given by

$$\phi_l(E,r)=[\cos\delta_l(E)]j_l[(E-V_0)^{1/2}r]-[\sin\delta_l(E)]n_l[(E-V_0)^{1/2}r] \tag{2.8}$$

for $r\geq S$, where $\delta_l(E)$ is the lth phase shift and V_0 is the muffin-tin zero of the potential. The integrations in (2.6) and (2.7) extend over the volume Ω of the primitive cell. For close-packed systems, however, they can be approximated with negligible error by integrations over the Wigner-Seitz (WS) sphere with radius $S_{\rm WS}$ given by $\Omega=4\pi S_{\rm WS}^3/3$.

Consider now a single muffin-tin potential confined in a sphere of radius $S_{\rm WS}$ embedded in a constant potential V_0. The corresponding spectrum for the core state c is also given by (2.5) but with $f_{c,l}(E)$ replaced by

$$f^{\rm at}_{c,l}(E)=(2l+1)N^{\rm FE}(E)\langle\phi_c\,|\,\vec{r}\,|\,\phi_l(E)\rangle^2\,, \tag{2.9}$$

where $N^{\rm FE}(E)=(E-V_0)^{1/2}/2\pi^2$ is the free-electron (FE) density of states (see Appendix C). As we argue below, for $E>0$, this spectrum is very close to the single-particle atomic spectrum and we shall refer to it as "atomiclike." Note that the normalization (2.8) of the partial waves is used in the single-particle problem to ensure an overall free-electron density of states. In the energy-band problem, on the other hand, this normalization is arbitrary and cancels out in the secular equation.

In order to make the connection between the solid-state and the single-sphere problems, it it convenient to introduce the projected density of states

$$N_l^{\rm at}(E)=\frac{1}{\Omega}(2l+1)N^{\rm FE}(E)\langle\phi_l^2(E)\rangle \tag{2.10}$$

for the single-sphere problem. Now we can rewrite (2.6) as

$$f_{c,l}(E)=f^{\rm at}_{c,l}(E)\frac{N_l(E)}{N_l^{\rm at}(E)}\,, \tag{2.11}$$

which provides the desired factorization of the spectra. In the remaining parts of this section, we interpret the ratio $N_l/N_l^{\rm at}$ as a solid-state contribution and identify the atomic strength $f^{\rm at}_{c,l}$ as an atomiclike (superscript "at") contribution to the spectrum.

B. Solid-state effects

We consider first free electrons with energy $E_{\vec{k}}=k^2-V_0$ described by plane waves

$$\psi_{\vec{k}}=\frac{4\pi}{\sqrt{\Omega}}\sum_{l,m} i^l Y^*_{lm}(\hat{k})Y_{lm}(\hat{r})j_l(kr)\ . \tag{2.12}$$

The projected density of states (2.7) inside a sphere of volume Ω becomes

$$N_l^{\rm FE}(E)=\frac{1}{\Omega}(2l+1)N^{\rm FE}(E)\langle j_l^2(E-V_0)\rangle\ , \tag{2.13}$$

where

$$\langle j_l^2(k^2)\rangle=4\pi\int_0^{S_{\rm WS}} dr\, r^2 j_l^2(kr)$$
$$=2\pi S_{\rm WS}^3[j_l^2(kS_{\rm WS})-j_{l-1}(kS_{\rm WS})j_{l+1}(kS_{\rm WS})]\ , \tag{2.14}$$

and it is shown in Fig. 1 for $l=0$–3.

The appropriate solutions for the single-sphere problem, with the same energies $E_{\vec{k}}$, are the APW's

$$\psi_{\vec{k}}=\frac{4\pi}{\sqrt{\Omega}}\sum_{l,m} i^l Y^*_{lm}(\hat{k})Y_{lm}(\hat{r})\phi_l(E_{\vec{k}},r)\ , \tag{2.15}$$

which yield the projected density of states $N_l^{\rm at}$ given by (2.10). The ratio of normalizations,

$$\frac{N_l^{\rm at}(E)}{N_l^{\rm FE}(E)}=\frac{\langle\phi_l^2(E)\rangle}{\langle j_l^2(E-V_0)\rangle}\ , \tag{2.16}$$

gives the change in the projected density of states due to the distortion of the wave function inside the atomic sphere. This effect, due entirely to the central potential, also determines the overall shape of $N_l(E)$ in the solid. This is illustrated in Fig. 2 where we show N_f and $N_f^{\rm at}$ for palladium, together with $N_f^{\rm FE}$ inside a sphere of radius $S_{\rm WS}$ appropriate for this element. Notice that all the projected densities of states defined over a finite volume Ω decrease at high energies. This is due to the increase of the number of nodes of the radial functions inside Ω with increasing energy. Notice also that N_l oscillates about the $N_l^{\rm at}$ of the central atom, the difference between them being the effect of the surrounding atoms. Therefore the ratio

$$\chi_l(E)=\frac{N_l(E)}{N_l^{\rm at}(E)}\ , \tag{2.17}$$

which factorizes out variations due to the normalization of the wave functions, represents a purely solid-state effect.

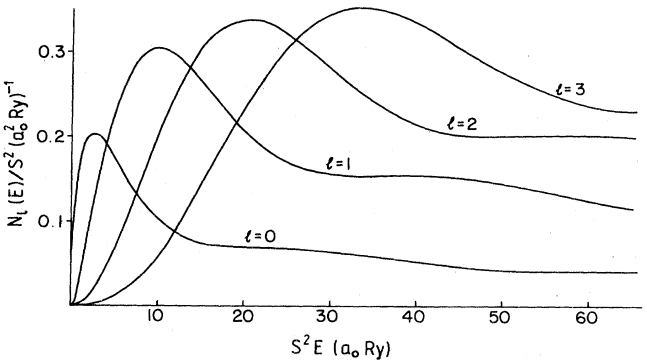

FIG. 1. Free-electron projected densities of states inside a sphere of radius S.

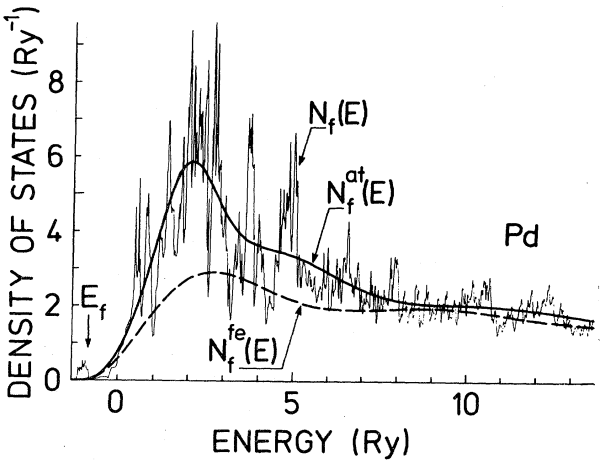

FIG. 2. Projected densities of states $N_l(E)$ and $N_l^{\rm at}(E)$ with $l=3$ for palladium, and $N_l^{\rm FE}(E)$ with $l=3$ inside a sphere of radius $S_{\rm WS}=2.83$ bohr, appropriate for palladium.

C. Atomiclike effects

The quantity $f_{c,l}^{\rm at}$ as defined by (2.8) and (2.9), is the oscillator strength appropriate to a single muffin tin embedded in a constant potential V_0. We have interpreted $f_{c,l}^{\rm at}$ as an atomiclike term because for energies $E>0$, which we are interested in, it is essentially equal to the corresponding single-particle atomic strength. This is illustrated in Fig. 3, where we have plotted $f_{c,l}^{\rm at}(E)$ together with the exact atomic strength for the 1s core state of Pd. At high energies, where the valence wave function is determined predominantly by the deeper part of the potential, the two curves agree. Near threshold, in the range $0>E>V_0$, the muffin-tin and the atomic spectra are qualitatively different. In this energy range the atom has a large number of bound np ($n=5,\ldots,\infty$) states, with decreasing oscillator strengths, which look like a continuum when the lifetime broadening is included, while the solid exhibits a single broad 5p band.

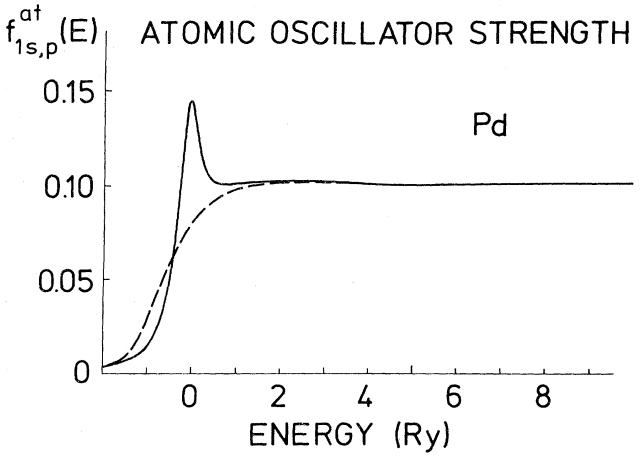

FIG. 3. Atomic oscillator strength for the 1s core state of palladium (solid line) and its muffin-tin approximation (dashed line). Both curves include the same core-state lifetime broadening (Table II).

The general energy dependence of the atomic oscillator strengths has been discussed in detail by Fano and Cooper.[20] For the case of localized core states, however, this dependence becomes particularly simple. The near-edge structure is dominated by the centrifugal barrier which produces a delayed or enhanced edge (also called a white line) when the values of the logarithmic derivative of the valence wave function at the Wigner-Seitz radius S_{WS} is positive or negative, respectively. For example, the $M_{4,5}$ spectrum of Pd exhibits a delayed edge which lies ~ 30 eV above the Fermi level, while the $L_{2,3}$ spectrum of all transition metals with unoccupied d states has white lines. Above the near-edge structure the atomic spectrum has a broad maximum at $E \simeq l(l+1)/S_{\mathrm{WS}}^2 + V_0$, and decreases slowly with increasing energy, due to the increasing curvature of the valence wave function in the core region.

III. ENERGY-BAND PROBLEM

Here we describe a linearized version of the APW method which can handle wide energy ranges. The central idea of the APW method is to decrease the number of plane waves needed to produce an accurate Bloch state by augmenting the plane waves with functions which have a more appropriate radial dependence over the core region.[22] In the linearized versions of the APW method, these radial functions are chosen to be independent of the energy of the Bloch state.[23] This leads to a linear secular equation for the crystal eigenvalues and eigenfunctions. In Andersen's original scheme, the augmenting functions are related to solutions of radial Schrödinger equation for the muffin-tin part of the potential with arbitrarily specified energies.[14] This scheme is therefore restricted to an energy range of one principal quantum number about these fixed energies.[24] By contrast, in the present scheme each partial term l of a plane wave is augmented with a solution of the radial Schrödinger equation whose energy $\epsilon_l(K)$ is related to the energy of the plane wave, K^2. In this way, the range of energies covered by the scheme is limited only by the number of plane waves included in the calculation. This feature is achieved at the price of keeping a larger number of parameters than in Andersen's method, namely the crystal potential functions $\epsilon_l(K)$. However, this is not a difficulty, since the calculation is to be performed on a computer.

A. Basis functions

Consider the problem of solving

$$(H - E_{\vec{\mathrm{k}}j})\psi_{\vec{\mathrm{k}}j}(\vec{\mathrm{r}}) = 0 , \tag{3.1}$$

with

$$H = -\nabla^2 + V(\vec{\mathrm{r}}) , \tag{3.2}$$

for a periodic muffin-tin potential $V(\vec{\mathrm{r}})$. We expand the Bloch wave function $\psi_{\vec{\mathrm{k}}j}$ for a state with reduced wave vector $\vec{\mathrm{k}}$ and band index j in terms of a set of basis functions $\chi_{\vec{\mathrm{K}}}$; that is,

$$\psi_{\vec{\mathrm{k}}j}(\vec{\mathrm{r}}) = \sum_{\vec{\mathrm{K}}} A_{\vec{\mathrm{K}}j}\chi_{\vec{\mathrm{K}}}(\vec{\mathrm{r}}) . \tag{3.3}$$

The index $\vec{\mathrm{K}}$ stands for

$$\vec{\mathrm{K}} = \vec{\mathrm{k}} + \vec{\mathrm{G}} , \tag{3.4}$$

so that the basis set is defined for each wave vector $\vec{\mathrm{k}}$, and is labeled by the reciprocal-lattice vector $\vec{\mathrm{G}}$. The basis functions are the energy-independent APW's defined by

$$\chi_{\vec{\mathrm{K}}}(\vec{\mathrm{r}}) = \begin{cases} 4\pi \sum_L Y_L^*(\hat{K})\, j_L(K,\vec{\mathrm{r}}) = e^{i\vec{\mathrm{K}}\cdot\vec{\mathrm{r}}}, & r \geq S \quad (3.5a) \\ 4\pi \sum_L Y_L^*(\hat{K})\, \phi_L(\epsilon_l(K),\vec{\mathrm{r}}) \dfrac{j_l(KS)}{\phi_l(\epsilon_l(K),S)}, & r \leq S \quad (3.5b) \end{cases}$$

where $S = S_{\mathrm{MT}}$ is the muffin-tin radius, and we have defined

$$j_L(K,\vec{\mathrm{r}}) = i^l Y_L(\hat{r}) j_l(Kr) \tag{3.6}$$

using the notation $L = l,m$. The wave function

$$\phi_L(\epsilon_l(K),\vec{\mathrm{r}}) = i^l Y_L(\hat{r})\phi_l(\epsilon_l(K),r) \tag{3.7}$$

is a solution of the Schrödinger equation

$$H\phi_L(E,\vec{\mathrm{r}}) = E\phi_L(E,\vec{\mathrm{r}}) \tag{3.8}$$

inside the muffin-tin sphere with fixed angular momentum quantum numbers L, and with the energy $E = \epsilon_l(K)$ determined by the logarithmic derivative boundary condition

$$D_l(\epsilon_l(K)) = D_l^{\mathrm{FE}}(K^2) , \tag{3.9}$$

where

$$D_l^{\mathrm{FE}}(K^2) = \left. \frac{x}{j_l(x)} \frac{dj_l(x)}{dx} \right|_{x=KS} \tag{3.10}$$

and

$$D_l(E) = \left. \frac{r}{\phi_l(E,r)} \frac{d\phi(E,r)}{dr} \right|_{r=S} . \tag{3.11}$$

In the interstitial region the energy-independent APW $\chi_{\vec{\mathrm{K}}}$ is defined to be the plane wave of wave vector $\vec{\mathrm{K}}$, and inside the muffin-tin sphere each of the partial components of the plane wave is augmented by a solution of the Schrödinger equation with energy chosen so that $\chi_{\vec{\mathrm{K}}}$ and its first derivative are continuous at the muffin-tin radius.

The set of crystal potential functions $\epsilon_l(K)$ for $l = 1,2,\ldots,$ defined by Eq. (3.9) contains all the informa-

tion about the spherically symmetric part of the potential which is relevant to the band-structure problem. These functions bear a simple numerical relation with the energy-dependent phase shifts $\delta_l(E)$ used in Sec. II A. While in Eq. (2.8) we have shifted the free-electron solution by δ_l outside the atomic sphere in order to have continuous and differentiably partial waves, here we shift the energy inside the muffin-tin sphere by $\epsilon_l(K)-K^2$ and retain the unshifted sinusoidal form of the plane waves in the interstitial region. The plane waves provide a very convenient way of fulfilling the periodic boundary condition by imposing the restriction (3.4) on our basis set. Note that $\chi_{\vec{K}}$, although it satisfies Bloch's theorem with Bloch vector $\vec{k}$, is not a solution of the Schrödinger equation for the solid because its energy $\epsilon_l(K)$ inside the muffin-tin sphere is different for each l and is also different from its energy K^2 in the interstitial region (except for the special case of free electrons).

B. Muffin-tin overlap integral

The overlap integral for the partial waves inside the muffin-tin sphere of radius S is given by

$$\langle\phi_L(E)\phi_{L'}(E')\rangle_{\rm MT} = -\delta_{LL'}S\phi_l(E,S)\phi_l(E',S)\frac{D_l(E)-D_l(E')}{E-E'} . \quad (3.12)$$

In order to prove this expression, we convert the volume integral into a surface integral using Green's theorem as follows:

$$(E'-E)\langle\phi_L(E)\phi_{L'}(E')\rangle_{\rm MT} = \langle\phi_L(E)H\phi_L(E')\rangle_{\rm MT}-\langle\phi_{L'}(E')H\phi_L(E)\rangle_{\rm MT} \quad (3.13)$$

$$= -\delta_{LL'}S^2\left[\phi_l(E,r)\frac{d}{dr}\phi_l(E',r) - \phi_l(E',r)\frac{d}{dr}\phi_l(E,r)\right]\Bigg|_{r=S} , \quad (3.14)$$

and we use the definition (3.11) of the logarithmic derivative $D_l(E)$.

C. Secular equation

The Schrödinger equation (3.1) can be obtained from the variational principle

$$\delta\langle\psi_{\vec{k}j}\,|\,(H-E_{\vec{k}j})\,|\,\psi_{\vec{k}j}\rangle=0 . \quad (3.15)$$

Substituting the trial wave function (3.3) into Eq. (3.15) and treating the expansion parameters $A_{\vec{k}j}$ as independent variational parameters leads to the secular equation

$$\sum_{\vec{K}'}(H_{\vec{K}\vec{K}'}-E_{\vec{k}j}O_{\vec{K}\vec{K}'})A_{\vec{K}'j}=0 , \quad (3.16)$$

where

$$H_{\vec{K}\vec{K}'}=\langle\chi_{\vec{K}}\,|\,H\,|\,\chi_{\vec{K}'}\rangle \quad (3.17)$$

and

$$O_{\vec{K}\vec{K}'}=\langle\chi_{\vec{K}}\,|\,\chi_{\vec{K}'}\rangle . \quad (3.18)$$

The secular equation (3.16) is linear in the energy simply because the basis functions $\chi_{\vec{K}}$ are independent of the energy $E_{\vec{k}j}$.

It is convenient to write the Hamiltonian and overlap matrices as

$$H_{\vec{K}\vec{K}'}-EO_{\vec{K}\vec{K}'}=\langle e^{-i\vec{K}\cdot\vec{r}}\,|\,(-\nabla^2-E)\,|\,e^{i\vec{K}'\cdot\vec{r}}\rangle_{\rm int} + \langle\chi_{\vec{K}}\,|\,(H-E)\,|\,\chi_{\vec{K}'}\rangle_{\rm MT} . \quad (3.19)$$

Here $\langle\ \rangle$, $\langle\ \rangle_{\rm int}$, and $\langle\ \rangle_{\rm MT}$ indicate integration over the primitive cell, the interstitial (subscript int) region, and the muffin-tin sphere, respectively. The subscripts $\vec{k}j$ in the energy eigenvalues and eigenfunctions will be omitted hereafter whenever there is no possibility for confusion.

The contribution from the muffin-tin sphere can be evaluated using (3.5b), (3.8), (3.12), and the addition theorem for the spherical harmonics, and one has

$$\langle\chi_{\vec{K}}\,|\,(H-E)\,|\,\chi_{\vec{K}'}\rangle_{\rm MT}=\Omega\sum_l W_l(\vec{K},\vec{K}')m_l(\vec{K},\vec{K}') \times[\epsilon_l(K')-E] , \quad (3.20)$$

where the quantity

$$W_l(\vec{K},\vec{K}')=\frac{4\pi S}{\Omega}(2l+1)P_l(\hat{K}\cdot\hat{K}')j_l(KS)j_l(K'S) \times\frac{D_l^{\rm FE}(K^2)-D_l^{\rm FE}(K'^2)}{K^2-K'^2} \quad (3.21)$$

is a geometrical factor which depends on the crystal structure but is independent of the potential, and

$$m_l(K,K')=\frac{K^2-K'^2}{\epsilon_l(K)-\epsilon_l(K')} \quad (3.22)$$

is a nondiagonal effective mass.

The contribution from the interstitial region can be written as the difference between the integral over the entire primitive cell and that over the muffin-tin sphere. The integral over the primitive cell is simply $\Omega(K^2-E)\delta_{\vec{K}\vec{K}'}$, since the plane waves $e^{i\vec{K}\cdot\vec{r}}$, with wave vectors $\vec{K}=\vec{k}+\vec{G}$, form an orthogonal set over that volume. The remaining integral over the muffin-tin sphere is a particular case of (3.20) with $\epsilon_l(K)=K^2$ and $m_l(K,K')=1$, so that

$$\langle e^{-i\vec{K}\cdot\vec{r}}\,|\,(-\nabla^2-E)\,|\,e^{i\vec{K}'\cdot\vec{r}}\rangle_{\rm int}=\Omega(K^2-E)\delta_{\vec{K}\vec{K}'}-\Omega\sum_l W_l(\vec{K},\vec{K}')(K'^2-E) . \quad (3.23)$$

From (3.20) and (3.23) one obtains the following expression for the secular matrix:

$$\frac{1}{\Omega}(H_{\vec{K}\,\vec{K}'}-EO_{\vec{K}\,\vec{K}'})=(K'^2-E)\delta_{\vec{K}\,\vec{K}'}+\sum_l W_l(\vec{K},\vec{K}')\{m_l(K,K')[\epsilon_l(K')-E]-(K'^2-E)\}\ . \tag{3.24}$$

The Hamiltonian and overlap matrices can be rewritten in the form

$$\frac{1}{\Omega}H_{\vec{K}\,\vec{K}'}=K^2\delta_{\vec{K}\,\vec{K}'}+\sum_l W_l(\vec{K},\vec{K}')\{\tfrac{1}{2}[\epsilon_l(K)+\epsilon_l(K')]m_l(K,K')-\tfrac{1}{2}(K^2+K'^2)\}\ , \tag{3.25}$$

$$\frac{1}{\Omega}O_{\vec{K}\,\vec{K}'}=\delta_{\vec{K}\,\vec{K}'}+\sum_l W_l(\vec{K},\vec{K}')[m_l(K,K')-1]\ , \tag{3.26}$$

which are explicitly Hermitian.

In practice, the l sum in (3.24) is necessarily terminated at some finite $l=l_{\max}$. Nevertheless, as in other APW schemes, the formalism automatically incorporates the remaining terms from $l=l_{\max}+1$ to $l=\infty$ with $\epsilon_l(K)=K^2$ and $m_l(K,K')=1$. Therefore, as long as the neglected terms are free-electron-like, this approximation entails no truncation errors. Note also, that for free electrons, the method becomes exact [cf. Eq. (3.24)].

D. Crystal potential functions

The crystal potential enters the Hamiltonian and overlap matrices through the potential functions $\epsilon_l(K)$, for $l=0,1,\ldots,$ etc. In our calculations, these functions are computed and tabulated for a discrete set of values of K^2, defined on a mesh chosen to have 100 points uniformly distributed within each n,l band. These are fed into the calculation as input data, and the specific values of $\epsilon_l(K)$ required to construct the secular equation are then obtained by numerical interpolation.

To construct these functions, we solve the implicit equation (3.9) numerically for each value of K^2 in the mesh. This is schematically illustrated in Fig. 4, where we note that $D_l(\epsilon_l)$ assumes the value $D_l^{\mathrm{FE}}(K^2)$ for infinite many values of ϵ_l. Each solution yields a different branch $\epsilon_l^{(n)}(K)$ of the crystal potential function. The different branches have been labeled with a superscript which indicates the value of the principal quantum number of the first band included in each branch. This means that the function $\epsilon_l^{(\nu)}(K)$, for instance, includes all the n,l bands with $n\geq\nu$. The use of these different branches to generate different energy panels will be discussed in Sec. IV. To keep the notation simpler, however, the superscript in the crystal potential functions will be omitted whenever there is no possibility for confusion.

The evaluation of the diagonal terms of the secular equation (3.24) requires special mention. For $K=K'$, one needs

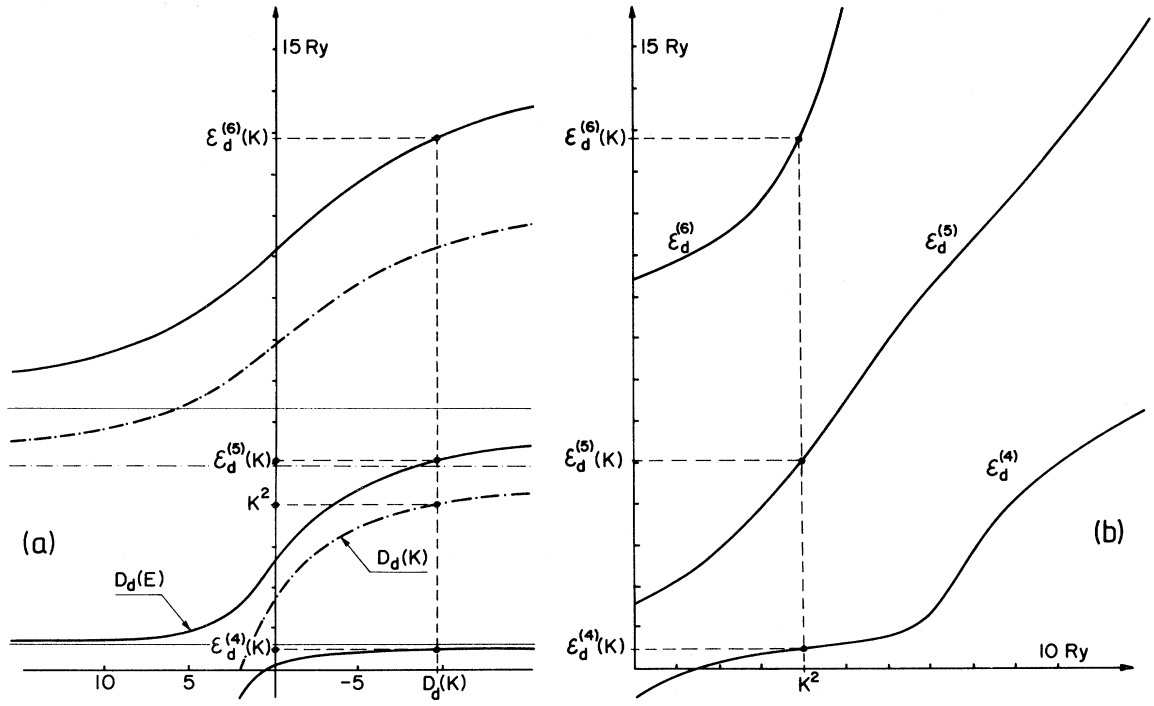

FIG. 4. Construction of the crystal potential functions. (a) The crystal-potential (solid line) and free-electron (dashed-dotted) logarithmic derivatives for the d bands of palladium. For each value of K, there are an infinite number of solutions $\epsilon_d^{(n)}(K)$ with the same logarithmic derivative $D_d(K)$. (b) The $n=4$, 5, and 6 branches of the crystal-potential functions for $l=2$.

$$W_l(K)=\frac{1}{\Omega}(2l+1)\langle j_l^2(K^2)\rangle_{\mathrm{MT}} \tag{3.27}$$

[cf. Eq. (3.21)], which has been evaluated using (3.12), and one also needs

$$m_l(K)=\frac{dK^2}{d\epsilon_l} \tag{3.28}$$

[cf. Eq. (3.22)]. Rather than using numerical differentiation of the function $\epsilon_l(K)$, it is more accurate to evaluate this last quantity via

$$m_l(K)=\frac{\langle\phi_l^2(\epsilon_l(K))\rangle_{\mathrm{MT}}/\phi_l^2(\epsilon_l(K),S)}{\langle j_l^2(K^2)\rangle_{\mathrm{MT}}/j_l^2(KS)}\ , \tag{3.29}$$

which follows from (3.9) and (3.12). The numerator of (3.29) can be easily obtained by numerical integration of the wave function $\phi_l(\epsilon_l(K),r)$, while for $\langle j_l^2(K^2)\rangle_{\mathrm{MT}}$ in (3.27) and (3.29) we use Eq. (2.14) evaluated at the muffin-tin radius $S=S_{\mathrm{MT}}$. In this paper we have evaluated $m_l(K)$ in a seperate calculation and furnished it as additional input data.

The crystal potential functions for the $4d$ and $6h$ branches of palladium are shown in Figs. 5 and 6, together with the corresponding diagonal effective masses $m_l(K)$.

E. Physical interpretation of the secular equation

In attempting to interpret this formalism, we first consider the effect of a single APW and then discuss the influence of the off-diagonal matrix elements.

The diagonal terms of the secular matrix (3.24) are given by

$$\frac{1}{\Omega}(H_{\vec{K}\,\vec{K}}-EO_{\vec{K}\,\vec{K}})=(1-\Omega_{\mathrm{MT}}/\Omega)(K^2-E)+\sum_l W_l(K)m_l(K)[\epsilon_l(K)-E]\ , \tag{3.30}$$

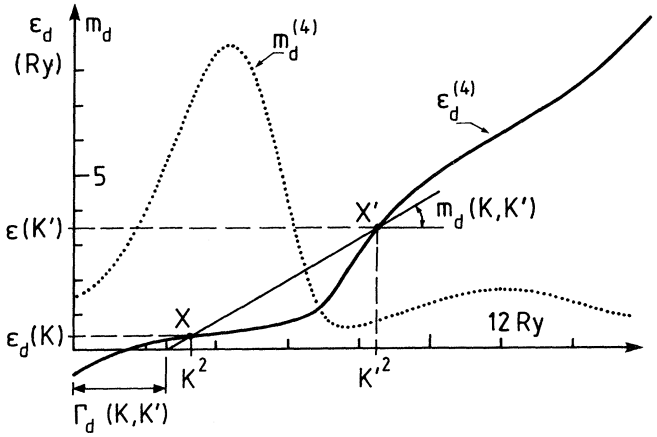

FIG. 5. Interpretation of a general crystal-potential function. The thick solid curve represents $\epsilon_d^{(4)}(K)$ for palladium. The pseudopotential $\Gamma_d(K,K')$ is given by the intersection of the straight (solid,thin) line through the points X and X' with the horizontal axis, and the nondiagonal effective mass $m_d(K,K')$ is the slope of this line. Also shown is the diagonal effective mass $m_d^{(4)}(K)=m_d(K,K)$.

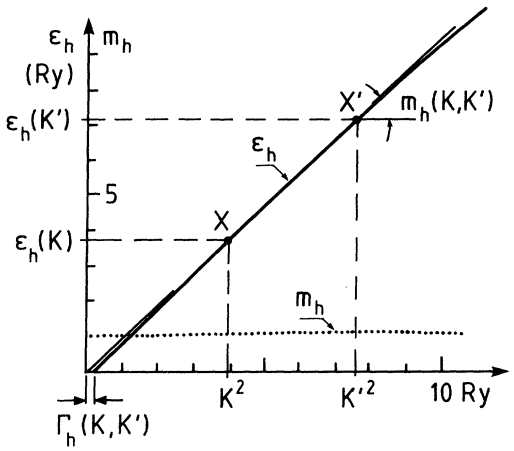

FIG. 6. Interpretation of a free-electron-like crystal-potential function. The plot of $\epsilon_h(K)$ as a function of K^2 is almost a straight line, and $m_h(K)\simeq 1$ for palladium. Accordingly, both the pseudopotential Γ_l and the overlap function Δ_l can be approximated by constants independent of K and K' for $l=5$. The same holds for $l>5$.

where the weight factor $W_l(K)$ is defined by Eq. (3.27) and satisfies the normalization condition

$$\sum_l W_l(K)=\frac{1}{\Omega}\langle e^{i(\vec{K}-\vec{K}')\cdot\vec{r}}\rangle_{\mathrm{MT}}=\frac{\Omega_{\mathrm{MT}}}{\Omega}\ . \tag{3.31}$$

By requiring that the diagonal terms vanish, one obtains the expectation value of the energy for the single energy-independent APW's, namely

$$E(K)=\frac{(1-\Omega_{\mathrm{MT}}/\Omega)K^2+\sum_l W_l(K)m_l(K)\epsilon_l(K)}{(1-\Omega_{\mathrm{MT}}/\Omega)+\sum_l W_l(K)m_l(K)}\ . \tag{3.32}$$

From (3.29) and (3.32) it follows that $E(K)$ represents the weighted mean of K^2 from the interstitial region and $\epsilon_l(K)$, for each l, from the muffin-tin sphere, the weights being given by the probabilities of finding the energy-independent APW in the interstitial region and muffin-tin sphere, respectively. In the actual band-structure calculation, as one scans all values of the Bloch vector $\vec{k}$ in the irreducible part of the Brillouin zone, each function $\epsilon_l(K)$ is sampled for all values of K with a weight given by $W_l(K)m_l(K)$. From (2.13) and (3.27) we observe that $W_l(K)$ is proportional to the projected density of states for free electrons $N_l^{\mathrm{FE}}(K^2)$ in the muffin-tin sphere. This means that the crystal potential functions with small- (large-) l components are sampled preferentially by the energy-independent APW's with small- (large-) K values, where the corresponding $N_l^{\mathrm{FE}}(K^2)$ in the muffin-tin sphere is large (cf. Fig. 1). Also, bands with larger effective masses $m_l(K)$ have larger weight in the secular equation.

To discuss the off-diagonal terms of the secular equation, it is convenient to rewrite (3.24) as

$$\frac{1}{\Omega}(H_{\vec{K}\,\vec{K}'}-EO_{\vec{K}\,\vec{K}'}) = (K^2-E)\delta_{\vec{K}\,\vec{K}'}+\sum_l W_l(\vec{K},\vec{K}')[\Gamma_l(K,K') - E\Delta_l(K,K')] . \tag{3.33}$$

The degree of mixing of the energy-independent APW's with wave vectors $\vec{K}$ and $\vec{K}'$ depends on the crystal structure and the potential. The dependence on the crystal structure is determined by the functions $W_l(\vec{K},\vec{K}')$ for each l, while the dependence on the potential is determined by the pseudopotential function

$$\Gamma_l(K,K')=m_l(K,K')\epsilon_l(K)-K^2 \tag{3.34}$$

in the Hamiltonian, and by the overlap function

$$\Delta_l(K,K')=m_l(K,K')-1 \tag{3.35}$$

in the overlap matrix.

A simple physical interpretation of $\Gamma_l(K,K')$ and $\Delta_l(K,K')$ is given in Figs. 5 and 6. Notice that the pseudopotential $\Gamma_l(K,K')$ is that constant potential which would make a free particle with orbital quantum number l and mass $m_l(K,K')$ have the energies $\epsilon_l(K)$ and $\epsilon_l(K')$ for wave vectors of magnitude K and K', respectively. Observe also that for the case of a general band, illustrated in Fig. 5 with the d band of palladium, the pseudopotential Γ_l has a complicated dependence on K and K', not susceptible to any simple mathematical approximations. On the other hand, for a free-electron-like band, as illustrated in Fig. 6 by the h ($l=5$) band of palladium, $\epsilon_l(K)$ plotted as a function of K^2 is almost a straight line. The behavior of the lth partial wave of the eigenstates is determined by the effective potential

$$V_l(r)=V(r)+\frac{l(l+1)}{r^2} \tag{3.36}$$

(see Fig. 7). For large l values, the centrifugal term $l(l+1)/r^2$ confines the corresponding partial wave to the outer region of the atom where $V(r)\simeq 0$. Since the centrifugal term is included exactly in the formalism, both the pseudopotential Γ_l and the overlap function Δ_l can be approximated by constants independent of K and K' for a large energy range. This approximation represents an important simplification for the bands at high energies, where large values of l are required. For free electrons, both Γ_l and Δ_l are identically zero for all l, so that the method is exact in that limit.

IV. PRACTICAL ASPECTS AND PERFORMANCE OF THE SCHEME

In order to illustrate the practical features and performance of the method developed in the preceding section, here we present the details of the calculation of the various x-ray spectra of palladium over an energy range of 10 Ry. Subsection A gives a cursory description of the entire calculation; the input and output of each step of the calculation are presented and briefly described. Then, in subsection B, the use of energy panels is discussed. As we shall see, it is not essential to use them, but they provide a convenient way of increasing the accuracy and computational speed. The convergence properties and practical accuracy to be expected from the band-structure scheme is discussed in subsection C, while the $\vec{k}$-space–integration method is described in subsection D. Finally, in subsection E, the broadening of the spectra in order to account for the finite lifetimes of the initial and final states is explained.

A. Overview of the calculation

The basic ingredient of any band-structure calculation is the crystal potential. The one used in the present calculation for palladium is a non-self-consistent muffin-tin potential constructed using the so-called Mattheiss prescription[25] (see Fig. 7). In general, the muffin-tin approximation is expected to introduce errors of the order of the potential step at the muffin-tin radius, which in this case is equal to 0.4 eV. This error can be neglected here since it is much smaller than the linewidth of the states involved in the x-ray-absorption process, which we are interested in. From the muffin-tin potential one can obtain the crystal potential functions following the procedure described in Sec. III D.

Although, in principle, the method can generate the band structure over an arbitrarily large energy range, in specific applications it may be convenient to subdivide the total range into smaller overlapping energy panels and to perform a separate calculation for each panel. The general arguments relating to the choice of energy panels are discussed in subsection B. In the application presented in this section, the range of energies of interest, which ex-

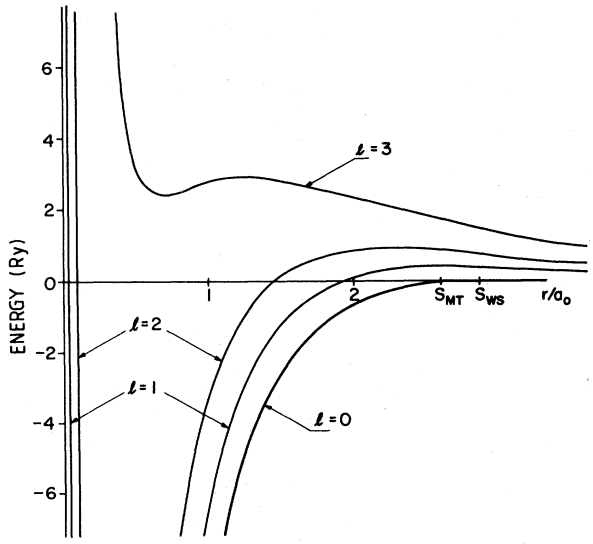

FIG. 7. Muffin-tin potential for palladium. The effective l-dependent potential $V_l(r)=V(r)+l(l+1)/r^2$ is presented for various values of l. The muffin-tin potential $V(r)$ has a step of 0.03 Ry at the muffin-tin radius S_{MT} not noticeable by the eye in this scale. The energies are referred to the muffin-tin zero $V_0=-1.29$ Ry.

tends from 0 to 10 Ry above the muffin-tin zero, has been subdivided into three panels. The relevant potential functions used each panel are indicated in Fig. 8. The first panel has been designed to accurately represent the states which arise from or are affected by the 4*d* band, and it is expected to yield the correct band structure over the range from 0 to 3 Ry. The second panel is intended to cover the energy range from 2 to 7 Ry, in which the band structure is mainly determined by the 4*f* band; the main difference is the use of the function $\epsilon_d^{(5)}$ instead of $\epsilon_d^{(4)}$ so that the second panel does not include the 4*d* bands. Also, since in this energy region $\epsilon_g^{(5)}$ begins to depart appreciably from free-electron behavior, it had to be included in the calculation. The third panel has been arranged, in a similar way, to leave out both the 4*d* and 4*f* bands.

In each panel, the calculation was performed for 256 $\vec{k}$ points in the irreducible $\frac{1}{48}$th wedge of the Brillouin zone. For each value of $\vec{k}$, on obtains the energies $E_{\vec{k}j}$ for $j=1,\ldots,d$, and the quantities

$$Q_l(\vec{k},j)=\int_0^{S_{\rm WS}} dr\, r^2 \sum_m |\langle Y_{lm}|\psi_{\vec{k}j}\rangle|^2 \tag{4.1}$$

$$=-\Omega \sum_{\vec{K},\vec{K}'} A^*_{\vec{K}j} A_{\vec{K}'j} \{W_l(\vec{K},\vec{K}')|_{\rm WS} - [m_l(K,K')-1] \times W_l(\vec{K},\vec{K}')\} \tag{4.2}$$

for $l=1,\ldots,l_{\max}$ and $j=1,\ldots,d$, where d is the number of basis functions used in the solution of the secular equation. Here $W_l(\vec{K},\vec{K}')|_{\rm WS}$ is given by (3.21) with Bessel functions and logarithmic derivatives evaluated at the Wigner-Seitz radius.

The resulting energy bands along the high-symmetry directions are shown in Fig. 9 for the first two panels. Observe that in the low-energy region, between 0 and 1 Ry, the second panel is inappropriate because the 4*d* bands are missing. However, in the range from 2 to 4 Ry the disagreement between the energies from the two panels is smaller than 0.04 Ry ($\simeq$0.5 eV). These discrepancies are a direct measure of the errors in the energies of the first panel due to the finite basis set; notice that, as expected from the use of the variational principle, the energies of the second panel lie always lower than those of the first one.

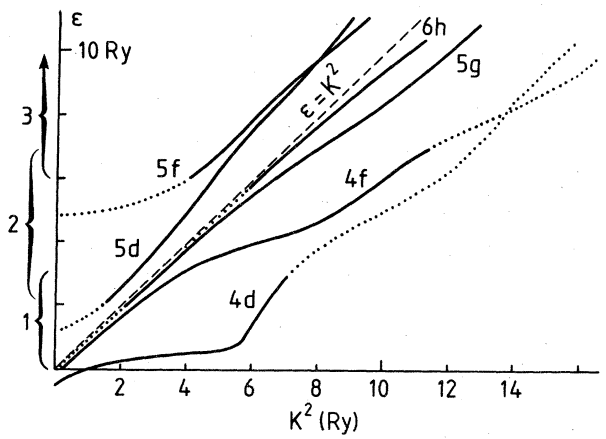

FIG. 8. Choice of energy panels. The crystal-potential functions for palladium used in panels 1, 2, and 3 are shown (solid lines). The functions $\epsilon_s^{(5)}$ and $\epsilon_p^{(5)}$ (omitted for clarity) have been employed in all three panels.

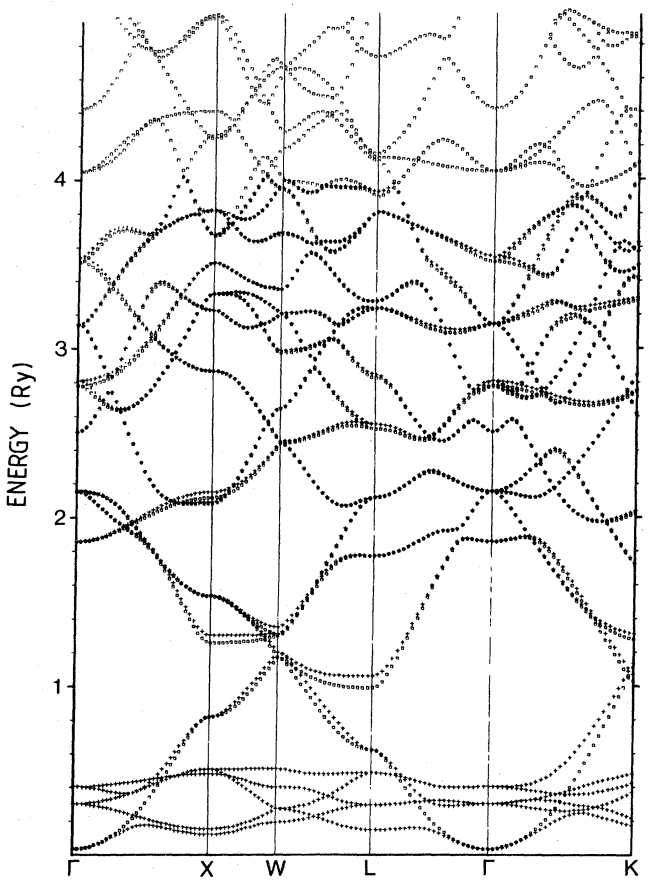

FIG. 9. Energy bands of fcc palladium for the first (pluses) and second (squares) panels along the high-symmetry directions. The energies are referred to the muffin-tin zero $V_0=-1.29$ Ry.

From the quantities $E_{\vec{k}j}$ and $Q_l(\vec{k},j)$ one can calculate the total and partial densities of states given by

$$N(E)=2\frac{\Omega}{(2\pi)^3}\sum_j \int d^3k\, \delta(E-E_{\vec{k}j}) \tag{4.3}$$

and

$$N_l(E)=2\frac{\Omega}{(2\pi)^3}\sum_j \int d^3k\, Q_l(\vec{k},j)\delta(E-E_{\vec{k}j}), \tag{4.4}$$

respectively, where the factor 2 "out front" comes from the spin sum. These integrations have been carried out by the method described in subsection D, using an energy step of 5 mRy for the first panel and 10 mRy for the other two panels. The first two panels of the function $N_p(E)$ are presented in Fig. 10. Notice that in the low-energy region the second panel misses the structure due to the 4*d* band. However, there is a range of energies from 1.5 to 4 Ry where the discrepancy between the two panels is quite

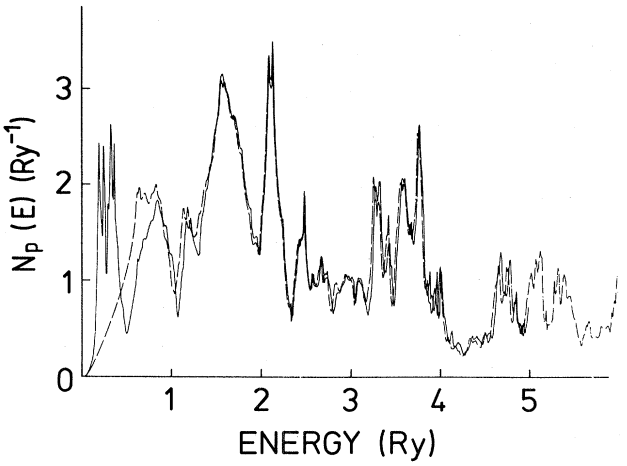

FIG. 10. First (solid line) and second (dashed line) panels of the $l=1$ projected density of states for palladium. The energies are referred to the muffin-tin zero $V_0=-1.29$ Ry.

small. These discrepancies give an indication of the error in the energy eigenvalues and in the $l=1$ part of the wave functions.

Since one can (and should) always arrange things so that two consecutive panels agree over a finite range of energies, the actual limits of each panel are not critical. Probably the best way to choose them is by visual inspection of the results plotted as in Fig. 10. In the calculation presented here the first panel was used from 0 to 3 Ry, the second from 3 to 7 Ry, and the third for energies above 7 Ry. The resulting total and partial densities of states are displayed in Fig. 11. We observe that these curves exhibit strong departures from the free-electron form (cf. Fig. 1), even several Ry above the Fermi level.

The calculation of the x-ray spectra has been discussed in Sec. II A, and the results are displayed in Fig. 12. The part of the spectra below E_F is proportional to the x-ray-emission intensity and that above E_F is proportional to the x-ray-absorption coefficient [cf. Eqs. (3) and (4)]. The absorption part has been broadened to account for the finite lifetime of the initial and final states in the manner described in subsection E. These results have been also included in Fig. 12.

Finally, the emission spectrum or the absorption coefficient can be calculated using Eqs. (3) or (4). In Fig. 13 the K-edge absorption coefficient has been presented together with the experimental results of Lengeler.[26]

B. Energy panels

The use of energy panels has been introduced not out of necessity but rather as a matter of convenience. It would have been possible to perform the calculation described in the preceding subsection with a single panel. To that end one would have used the branches $5s$, $5p$, $4d$, $4f$, $5g$, etc., of the crystal potential functions. In order to sample these functions from 0 to 10 Ry, one should have included in the calculation all the reciprocal-lattice vectors with at least $|\vec{G}|^2 \leq 17$ Ry (see Fig. 8). The dimension of the corresponding secular problem is, then, approximately given by

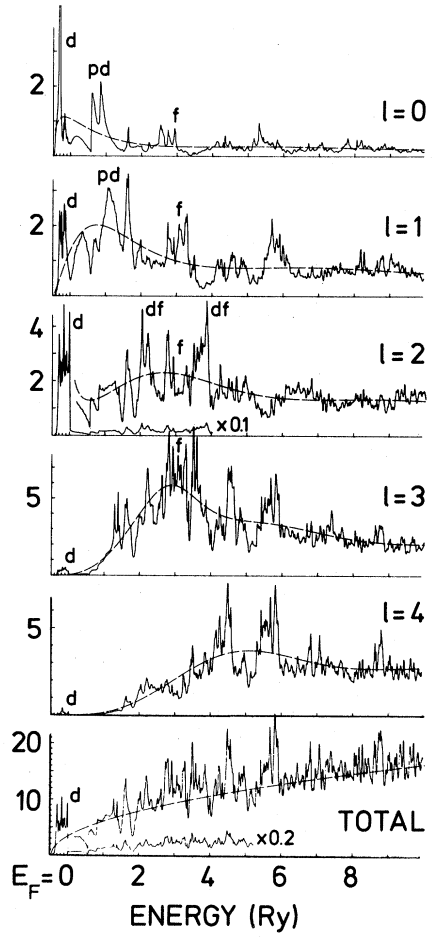

FIG. 11. Total and the $l=0$–4 projected densities of states (solid lines) for palladium are shown together with the free-electron total density of states $N^{FE}(E)$ and the projected densities of states $N_l^{at}(E)$, for the single-sphere problem (dashed lines). The energies are referred to the Fermi level $E_F=-0.80$ Ry, and the units of the vertical axis are states per atom per Ry.

$$d=\frac{(4\pi/3)G_{\max}^3}{(2\pi)^3/\Omega}=\frac{2}{9\pi}\nu(S_{WS}G_{\max})^3\,, \tag{4.5}$$

where S_{WS} is the Wigner-Seitz radius and ν is the number of atoms in the primitive cell, of volume Ω. In the present case $S_{WS}=2.87$ bohr and $\nu=1$ for fcc palladium, so that at least 120 reciprocal lattice vectors would have been required. We observe in Fig. 8 that this number is determined by the presence of the narrow $4d$ and $4f$ bands.

We now consider the calculation described in the preceding subsection, in which three panels were employed. For the first panel, which extends from 0 to 3 Ry, it is $G_{\max}^2 \simeq 7$ Ry (see Fig. 8), so that, by the argument presented above, the minimum dimension required for the secular equation is $d_1=31$. The second panel extends up to 7 Ry but utilizes the $5d$ rather than the $4d$ branch of the $l=2$ crystal potential function. Thus $G_{\max}$ is now determined by the $4f$ crystal potential function, so that one has $G_{\max}^2=11.5$ Ry, which yields $d_2=65$. The third panel does not include either the $4d$ or the $4f$ branches, so

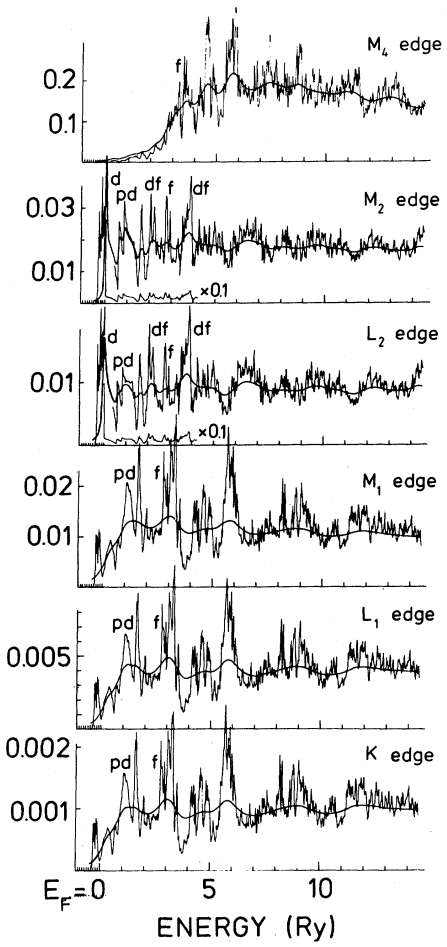

FIG. 12. K, L_1, M_1, L_2, M_2, and M_4 raw spectra for palladium are represented by the thin solid lines. The thick solid lines illustrate the absorption spectra broadened to account for the initial- and final-state linewidths. The energies are referred to the Fermi level $E_F=-0.80$ Ry, and the units of the vertical axis are Ry^{-1}.

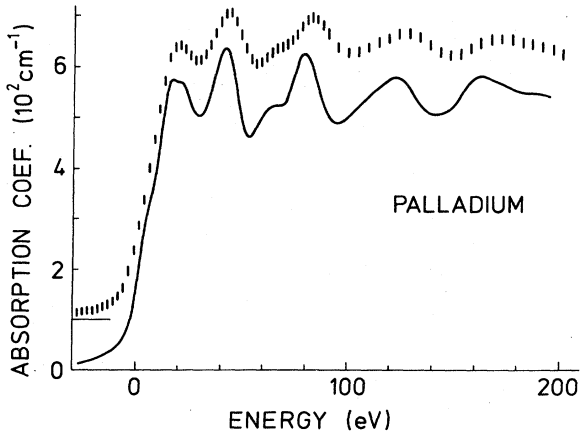

FIG. 13. Calculated K-edge absorption coefficient of palladium (continuous line) compared with the experimental results of Lengeler (discrete line).

that at 10 Ry one has $G^2_{\max}=12$ Ry, from which $d_3=70$.

The number of operations involved in a matrix diagonalization scales as the third power of its dimension. Therefore, since $31^3+65^3+70^3\cong 87^3<120^3$, it turns out that performing the calculation in three panels is computationally faster than using a single, larger panel.

Another reason for using panels is to improve the practical accuracy of the eigenvalues and eigenfunctions. For a given state, the error introduced by the variational principle increases with the number of lower-energy states included in the calculation, and is therefore smallest for the first few bands included in each panel. This point is more quantitatively discussed in the next subsection.

C. Convergence properties and practical accuracy

The results of a convergence test of the method for the energy bands of palladium, over an energy range of 10 Ry, are exhibited in Fig. 14. The test was carried out for a single low-symmetry point in the Brillouin zone with Bloch vector $\vec{k}=(\pi/4a,\ \pi/4a,\ 0)$, that is $\frac{1}{6}$th of the distance along the line ΓK, and only for a few eigenstates. These were selected because they were particularly "badly behaved," so that the conclusions of this subsection correspond to a "worst-case" situation. For the present analysis, the correct energies will be taken to be those computed with a secular equation of dimension $d=160$

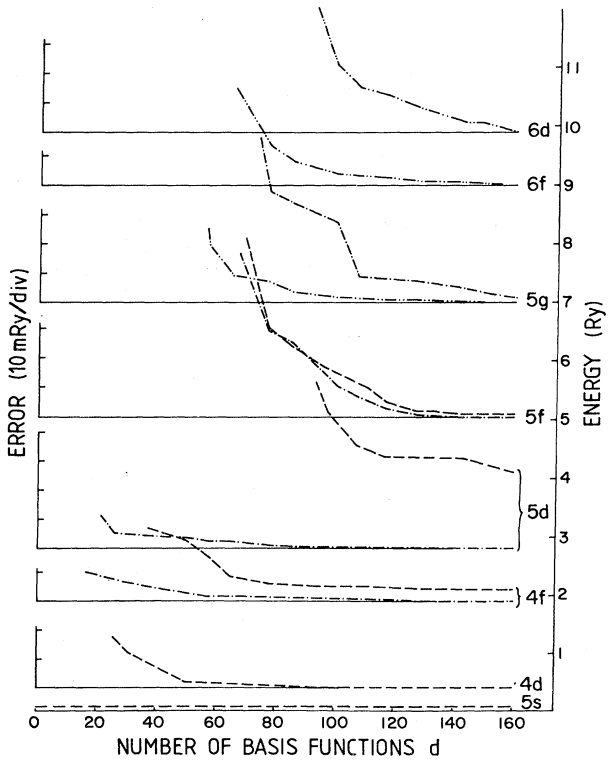

FIG. 14. Convergence test for palladium. The error in the energies as a function of the dimension d of the secular equation is presented for a selected (worst-case) set of eigenstates from the first (— — —), second (—·—·—·), and third (—··—··) panels. The eigenvalues for $d=160$ have been taken as the correct energies and are represented by horizontal solid lines.

and from the panel which gives the lowest values. These correct energies are represented in Fig. 14 by horizontal solid lines, and the errors are given, in an expanded scale, with respect to these reference lines.

We observe that the criterion (4.5) presented in the preceding subsection for the minimum dimension of the secular equation actually gives the minimum number of reciprocal-lattice vectors required to obtain reasonable results. According to that prescription the energies are correct only to 15 mRy, and if one reduces the value of d further they become quite wrong. On the other hand, in order to obtain energies correct to within 1 mRy, one has to take approximately twice as many basis functions.

Notice also how the presence of localized, and therefore narrow, states tends to reduce the accuracy of higher-energy bands with the same orbital symmetry. For instance, with $d=160$ the $5d$ band of the first panel shown in Fig. 14 is in error by 26 mRy, while in the second panel the same band is accurate within 2 mRy with only $d=60$. It should be mentioned, with reference to Fig. 8, that in all cases where the discrepancy between the energies from the two different panels is appreciable (noticeable by eye), the corresponding eigenstates have mostly $l=2$ character.

Thus we conclude that it is advantageous (faster and more accurate) to compute the contribution to the band structure from narrow bands in separate panels. In the case of palladium, there are two nonoverlapping narrow bands, the $4d$ and $4f$, and so two special panels have been chosen.

D. $\vec{k}$-space integration

The density-of-states integral (4.3) can be conveniently expressed as

$$N(E)=\frac{2\Omega}{(2\pi)^3}\sum_j \int \frac{dA}{|\vec{\nabla}_{\vec{k}} E_j(\vec{k})|}\Bigg|_{E_j(\vec{k})=E} . \tag{4.6}$$

Dividing the irreducible part of the Brillouin zone into microcells filling the entire region, the surface integral (4.6) can be evaluated as

$$N(E)=\frac{2\Omega}{(2\pi)^3}\sum_{c,j}\frac{A_{cj}(E)}{|\vec{\nabla}_{\vec{k}} E_j(\vec{k}_c)|} . \tag{4.7}$$

Here $A_{cj}(E)$ is the area of the surface of energy E inside the cth microcell, and $|\vec{\nabla}_{\vec{k}} E_j(\vec{k}_c)|$ is the magnitude of the energy gradient at the center of the microcell for the jth band.

Similarly, the projected densities of states (4.4) are given by

$$N_l(E)=\frac{2\Omega}{(2\pi)^3}\sum_{c,j} Q_l(\vec{k}_c,j)\frac{A_{cj}(E)}{|\vec{\nabla}_{\vec{k}} E_j(\vec{k}_c)|} , \tag{4.8}$$

where the quantity $Q_l(\vec{k}_c,j)$ is also evaluated at the center of the microcell.

The contribution of each microcell can be expressed in terms of the energies at the corners of the microcell, for each band. For a tetrahedral microcell of volume V, this contribution is given by[27]

$$\frac{A_{cj}(E)}{|\vec{\nabla}_{\vec{k}} E_j(\vec{k}_c)|}=\begin{cases} 3V\dfrac{(E-E_1)^2}{\Delta_{21}\Delta_{31}\Delta_{41}}, & E_1<E<E_2 \\ 3V\left[\dfrac{(E-E_1)^2}{\Delta_{21}\Delta_{31}\Delta_{41}}+\dfrac{(E-E_2)^2}{\Delta_{12}\Delta_{32}\Delta_{42}}\right], & E_2<E<E_3 \\ 3V\dfrac{(E-E_4)^2}{\Delta_{41}\Delta_{42}\Delta_{43}}, & E_3<E<E_4 \end{cases} \tag{4.9}$$

where E_1, E_2, E_3, and E_4 are the corner energies arranged in increasing order and $\Delta_{ij}=E_i-E_j$.

The simplest way to implement this scheme is by the interpolation approach: All quantities are calculated at the vertices of the tetrahedra and labeled consecutively according to increasing value of the energy. In applying (4.9) one then assumes that quantities with the same label belong to the same band. However, when two or more bands cross inside the microcell, this procedure gives an incorrect assignment of the corner energies. In order to circumvent this difficulty, we have used an extrapolation approach.[28] The secular equation was diagonalized for a set of Bloch vectors $\vec{k}=\vec{k}_c$, defined at the center of each tetrahedron, and the energies $E_j(\vec{k}_i)$ at the corners $\vec{k}_i$ were obtained using perturbation theory as

$$E_j(\vec{k}_i)=E_j(\vec{k}_c)+(\vec{k}_i-\vec{k}_c)\cdot\sum_{\vec{K},\vec{K}'} A^*_{\vec{K}j}A_{\vec{K}'j}\left[\frac{d}{d\vec{k}}H_{\vec{K}\vec{K}'}(\vec{k})-E_j(\vec{k})\frac{d}{d\vec{k}}O_{\vec{K}\vec{K}'}(\vec{k})\right]_{\vec{k}=\vec{k}_c} , \tag{4.10}$$

where $E_j(\vec{k}_c)$ and $A_{\vec{K}j}$ are the energy eigenvalues and eigenvectors at the corner of the tetrahedron. Equation (4.10) permits us to assign the band indices consistently to the four corners of the tetrahedron.

Figure 15 shows a comparison of the interpolation and extrapolation methods applied to the free-electron density of states. Observe that the interpolation method produces a spurious singularity at each band crossing. This effect also occurs in crystalline solids at high energies where the energy bands are rather free-electron-like. Another convenient feature of the extrapolation method is that each tetrahedron contributes separately to the integral, i.e., one does not have to store the eigenvalues and eigenfunctions. On the other hand, the method is more time consuming than the interpolation scheme because of the evaluation of (4.10).

E. Lifetime broadening

In the discussion presented so far, both the core hole and the excited electron produced in the photoabsorption

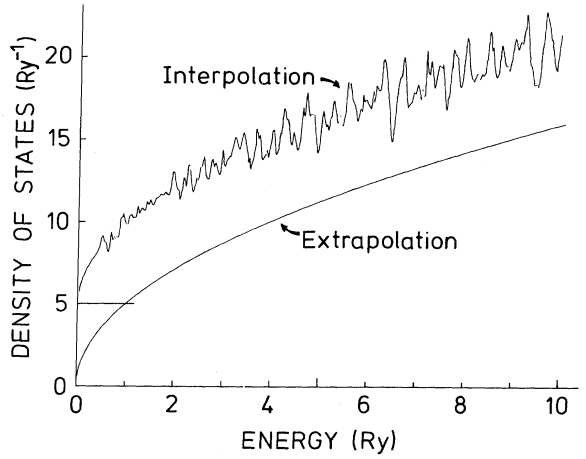

FIG. 15. Comparison of the interpolation and extrapolation $\vec{k}$-space–integration methods for free-electron bands. The density of states of an empty lattice, with the lattice spacing of palladium, has been evaluated using 256 tetrahedrons in the irreducible part of the Brillouin zone.

process have been assumed to have an infinite lifetime, and thus the initial and final energies of the electronic transition have been taken to be sharp. This assumption leads to the one-body spectra displayed in Fig. 12 (thin lines) which exhibit a distinct structure which is a rapidly varying function of energy. Experimentally it is found, however, that the initial and final states do have finite lifetimes. The core hole decays by radiative or Auger electronic transitions from some occupied higher-energy shells, while the excited electron loses energy by emitting plasmons or creating electron-hole pairs until it falls to the Fermi level. These finite lifetimes give to the initial and final states a Lorentzian line shape which manifests itself as a broadening of the spectra. This effect can be incorporated in the single-particle results by convoluting them with a Lorentzian function of the corresponding width. The broadening of the absorption spectrum due to the core-hole width Γ_c is given by

$$\bar{F}(E)=\frac{\Gamma_c}{2\pi}\int_{-\infty}^{\infty}\frac{F(E')dE'}{(E-E')^2+\frac{1}{4}\Gamma_c^2}\ , \tag{4.11}$$

while that due to the final-state width $\Gamma_x(E)$, which is energy dependent, produces an additional broadening which can be represented by

$$\bar{\bar{F}}(E)=\frac{1}{2\pi}\int_{-\infty}^{\infty}\frac{\Gamma_x(E')\bar{F}(E')dE'}{(E-E')^2+\frac{1}{4}\Gamma_x(E')^2}\ . \tag{4.12}$$

For the core-hole linewidth there exist both theoretical and experimental values[29] which are in rather good agreement. The ones used in this work are listed in Table II. For the final-state width, rather few values have been reported in the literature (either theoretical or experimental). The $\Gamma_x(E)$ utilized in this work has been estimated[15] by interpolation from the available compilations.[30]

TABLE II. Linewidths of the atomic energy levels for palladium (in eV).

K				
6.8				
L_1		L_2		L_3
6		1.9		2
M_1	M_2	M_3	M_4	M_5
8	0.5	1	0.4	0.3

V. PHYSICAL INTERPRETATION OF THE SPECTRA

The crucial result, proved in Appendix B, is that one-electron spectra due to core excitations factorize into atomic and solid-state terms. The atomic term determines the overall amplitude and shape of the spectra. It has a rather smooth energy dependence (cf. Sec. II C) and varies rather weakly with the atomic number Z. By contrast, the solid-state term has a rapidly varying energy dependence which is characteristic of the band structure of the system and which shows itself as oscillations about the atomic term.

In Fig. 12 we present the raw spectra together with the broadened absorption spectra for palladium. The spectra having the same solid-state factor look very similar: the K, L_1, and M_1 spectra involve the p final states of the conduction band; the L_2, L_3, M_2, and M_3 spectra involve the d (and to a lesser extent, the s) final states; and the M_4 and M_5 involve the f (and to a lesser extent, the p) final states. Here we neglect the spin-orbit coupling of the band states, which is expected to be negligible for palladium and lighter elements. The L_3, M_3, and M_5 spectra are not shown in Fig. 12, since we find that $F_{L_3}=2.09F_{L_2}$, $F_{M_3}=2.45F_{M_2}$, and $F_{M_5}=1.53F_{M_4}$, the departures from the statistical ratios of 2, 2, and 1.5, respectively, being due to differences in the corresponding atomic factors. Furthermore, the K, L_1, and M_1 spectra, as well as the L_2 and M_2 spectra, are distinguished only by differences in the atomic factor, the latter being more constant as a function of energy for the deeper core states.

The band structure of palladium is dominated by two narrow bands: the $4d$ band, which is mostly occupied, and the $4f$ band, which lies about 25 eV above the Fermi level. This last feature, namely the existence of a non-free-electron $4f$ band far above the Fermi level, is the main characteristic of the metals of the $4d$ row, which distinguish them from those of the $3d$ row. The physical origin of this effect is illustrated in Fig. 7 where we show the effective potential $V_l(r)=V(r)+l(l+1)/r^2$ for the partial waves of palladium. As a result of the competing effects of the attractive electrostatic potential $V(r)$ and of the centrifugal term $l(l+1)/r^2$, the function $V_f(r)$ becomes rather flat for $E\sim 2$ Ry, giving rise to a large effective mass [cf. Eq. (3.28)] and to a large density of states $N_f^{\rm at}(E)$

(cf. Fig. 3) at that energy. The $4f$ band, which in the rare-earth metals is known to give rise to sharp states near the Fermi level, begins in the $4d$ series to "peel off" from the continuum and to become a narrower band.

Many of the features of the band-structure results of Fig. 11 can be explained in terms of hybridization between the different n,l bands. In the presence of narrow bands, a description in terms of canonical densities of states is most appropriate.[13] The canonical densities of states[14] contain the full crystal-structure data but no information on mixing between the different l components. For a narrow band the corresponding partial density of states is essentially equal to the canonical one, almost unaffected by the other n,l bands. The narrow band does, however, affect all the other partial densities of states by means of two mechanisms: (i) the lighter states (which usually have an angular momentum l less than that of the narrow band) are pushed away from the narrow band, producing a suppression in the corresponding partial densities of states, and (ii) all the other partial densities of states exhibit a replica of the density of states of the narrow band. This latter effect arises from the tails of the orbitals of the narrow band centered in adjacent sites. Viewed from the central atom, these tails have, in general, a finite projection on all values of the angular momentum, leading to the above-mentioned structure.

In the case of palladium the $4d$ band lies between 0 and -4.75 eV with respect to the Fermi level. This narrow band gives rise to a large d density of states, a feature indicated by d in Figs. 11 and 12. A replica of d can be seen in all the other partial densities of states. There is also a suppression of the s and p densities of states just above the d feature. The states pushed away by the $4d$ band pile up in a peak above the d suppression, which we have denoted pd.

On the other hand, the $4f$ band is broader than the $4d$ band and gives rise to weaker features, indicated by f in Figs. 11 and 12. It interacts mostly with the $5d$ band, producing a suppression in the d density of states. The d states pushed away by the $4f$ band pile up in two peaks denoted by df in Fig. 11. The replica of the f features can be seen in the s and p densities of states followed by a suppression due to the upper df peak.

Features in the solid-state term lying at higher energies cannot be explained simply in these terms. There, it is more appropriate to apply the EXAFS approach[2] where one thinks of the final-state wave functions as being localized by the first few shells of the neighboring atoms.

ACKNOWLEDGMENTS

Part of this work, included in Ref. 16, was supported by the Materials Science Center at Cornell University under a grant from the National Science Foundation. We gratefully acknowledge the initiating stimulus on the linearized APW method of O. K. Andersen, the assistance by O. Jepsen with many aspects of the computation, and the timely and stimulating comments of A. R. Williams.

APPENDIX A: ATOMIC RYDBERG UNITS

The units in the atomic Rydberg system are composed of various combinations of the charge $(-e)$ and the mass m_0 of the electron and of Planck's constant $\hbar$. They are given as follows.

(i) The unit of mass is $2m_0=1.821\,906\times10^{-27}$ g.
(ii) The unit of charge is $e/\sqrt{2}=3.396\,411\times10^{-10}$ esu.
(iii) The unit of length is $a_0=\hbar^2/e^2m_0=5.291\,772\times10^{-9}$ cm.
(iv) The unit of energy is $\mathrm{Ry}=e^2/2a_0=2.179\,914\times10^{-11}$ erg $=13.605\,823$ eV.
(v) The unit of angular momentum is $\hbar=1.054\,592\times10^{-27}$ erg sec.

In this system of units the energy of a free electron of wave number $\vec{k}$ is given by $E=k^2$, and that of the static Coulomb energy at a distance r of a nucleus of atomic number Z is given by

$$V(r)=2Z/r\ . \tag{A1}$$

Notice also that the velocity of light is given by $c=2\alpha^{-1}=274.072$, where α is the fine-structure constant.

APPENDIX B: FACTORIZATION OF THE SPECTRUM INTO PROJECTED DENSITIES OF STATES AND ENERGY-DEPENDENT MATRIX ELEMENTS

As a first step to deriving the factorized expression for the x-ray spectra we introduce l,J-projected densities of states appropriate for the case of spin-orbit coupling. In this case it is convenient to write the crystal wave function in terms of eigenfunctions $|\,l,J,M\rangle$ of the total angular momentum $\vec{J}=\vec{L}+\vec{s}$ as

$$\psi_{\vec{k}j}(\vec{r})=4\pi\sum_{\vec{k},\sigma}\sum_{l,m}A^{j}_{\vec{k}\sigma}\,i^l Y^*_{lm}(\hat{K})\,j_l(KS)\sum_{J=l\pm1/2}\beta_J(l,m,\sigma)\frac{\phi_{lJ}(\epsilon_{lJ}(K),r)}{\phi_{lJ}(\epsilon_{lJ}(K),S)}\,|\,l,\,J,\,m+\sigma\rangle\ , \tag{B1}$$

with

$$\beta_{J=l\pm1/2}(l,m,\sigma)=2\sigma\left[\frac{J+2\sigma m\pm\frac{1}{2}}{2l+1}\right]^{1/2}\ , \tag{B2}$$

where we notice that the crystal potential functions are also labeled by l,J. The wave function can be rewritten as

$$\psi_{\vec{k}j}(\vec{r})=\sum_{l,J,M}\phi_{lJM}(\vec{k},j;r)\,|\,l,J,M,\rangle\ , \tag{B3}$$

where the vectors $|l,J,M\rangle$ contain all the angular and spin dependence, and $\phi_{lJM}(\vec{k},j;r)$ is a spherically symmetric wave function. Since $H\psi_{\vec{k}j}=E_{\vec{k}j}\psi_{\vec{k}j}$, the function $\phi_{lJM}(\vec{k},j;r)$ is a solution of the radial Pauli equation at the same energy $E_{\vec{k}j}$, that is

$$\phi_{lJM}(\vec{k},j;r)=\alpha_{lJM}(\vec{k},j)\phi_{lJ}(E_{\vec{k}j},r) , \tag{B4}$$

where the normalization coefficients $\alpha_{lJM}(\vec{k},j)$ are connected to the amplitudes $A^{j}_{\vec{K}\sigma}$ by

$$\alpha_{lJM}(\vec{k},j)=4\pi i^{l}\sum_{\vec{K},\sigma}A^{i}_{\vec{K}\sigma}\frac{j_l(KS)}{\phi_{lJ}(E_{\vec{k}j},S)}\sum_{m}\beta_J(l,m,\sigma)Y^{*}_{lm}(\hat{K}) . \tag{B5}$$

In this representation the new projected densities of states are given by

$$N_{lJ}(E)=\sum_{\vec{k},j}\delta(E-E_{\vec{k}j})\sum_{M}|\langle l,J,M\,|\,\psi_{\vec{k}j}\rangle|^{2} \tag{B6}$$

$$=\langle\phi^{2}_{lJ}(E)\rangle\sum_{\vec{k},j}\delta(E-E_{\vec{k}j})\sum_{M}|\alpha_{lJM}(\vec{k},j)|^{2} , \tag{B7}$$

where in the integration we have again replaced the primitive cell by a sphere of radius $S_{\rm WS}$, so that

$$\langle\phi^{2}_{lJ}(E)\rangle=\int_{0}^{S_{\rm WS}}dr\,r^{2}\phi^{2}_{lJ}(E,r) . \tag{B8}$$

The contribution to the spectrum $F_c(E)$, which corresponds to a core state $c=(n,l,J)$, is given by

$$\frac{3}{\omega}F_{n,l,J}(E)=\sum_{\vec{k},j}\delta(E-E_{\vec{k}j})\sum_{M}|\langle n,l,J,M\,|\,\vec{r}\,|\,\psi_{\vec{k}j}\rangle|^{2} \tag{B9}$$

$$=\sum_{\vec{k},j}\delta(E-E_{\vec{k}j})\sum_{\substack{l',J',M',\\ l'',J'',M''}}\alpha^{*}_{l'J'M'}(\vec{k},j)\alpha_{l''J''M''}(\vec{k},j)$$

$$\times\sum_{M}\langle E,l',J',M'\,|\,\vec{r}\,|\,n,l,J,M\rangle\cdot\langle n,l,J,M\,|\,\vec{r}\,|\,E,l'',J'',M''\rangle , \tag{B10}$$

where we have denoted $|E,l,J,M\rangle=\phi_{lJ}(E)\,|\,l,J,M\rangle$. The M sum in (B10) can be evaluated using Eq. (13^{3}.1) of Condon and Shortley[31] to obtain

$$\frac{3}{\omega}F_{n,l,J}(E)=\sum_{l'}\sum_{J'=l'\pm1/2}(E,l',J'\,|\,r\,|\,n,l,J)^{2}\Theta(J',J)\sum_{\vec{k},j}\delta(E-E_{\vec{k}j})\sum_{M}|\alpha_{l'J'M'}(\vec{k},j)|^{2} \tag{B11}$$

$$=(2J+1)\sum_{l'}\sum_{J'=l'\pm1/2}\frac{(E,l',J'\,|\,r\,|\,n,l,J)^{2}\Theta(J,J')}{\langle\phi^{2}_{l'J'}(E)\rangle}\frac{N_{l'J'}(E)}{2J'+1} , \tag{B12}$$

where

$$\frac{(E,l',J'\,|\,r\,|\,n,l,J)^{2}\Theta(J,J')}{\langle\phi^{2}_{l'J'}(E)\rangle}=\tfrac{1}{4}r^{2}_{l'J'}(E)\begin{cases}1/J(J+1), & J'=J\\ (2J-1)/J, & J'=J-1\\ (2J+3)/(J+1), & J'=J+1\end{cases} \tag{B13}$$

where

$$r_{l'J'}(E)=\langle\phi^{2}_{l'J'}(E)\rangle^{-1/2}\int_{0}^{S_{\rm WS}}dr\,r^{2}\phi_{nlJ}(r)r\phi_{l'J'}(E,r) \tag{B14}$$

are the reduced matrix elements of the Wigner-Seitz-Eckart theorem, and we have used the fact that

$$(2J'+1)\Theta(J',J)=(2J+1)\Theta(J,J') . \tag{B15}$$

Therefore, one has

$$\frac{3}{\omega}F_{n,l,J=l\pm1/2}(E)=\frac{1}{4}\left[\frac{2J+1}{J}r^{2}_{l-1,J-1}(E)N_{l-1,J-1}(E)+\frac{1}{J(J+1)}r^{2}_{l\pm1,J}(E)N_{l\pm1,J}(E)\right.$$

$$\left.+\frac{2J+1}{J+1}r^{2}_{l+1,J+1}(E)N_{l+1,J+1}(E)\right] . \tag{B16}$$

If we neglect the spin-orbit coupling, the integrals $r_{lJ}(E)$ become independent of J, the appropriate projected densities of states are

$$N_l(E)=\frac{2(2l+1)}{2J+1}N_{lJ}(E)\ , \tag{B17}$$

and the spectrum (B16) becomes

$$\frac{3}{\omega}F_{n,l,J}(E)=\frac{2J+1}{2(2l+1)}\left[(l+1)r^2_{l+1}(E)\frac{N_{l+1}(E)}{2l+3}+lr^2_{l-1}(E)\frac{N_{l-1}(E)}{2l-1}\right]\ . \tag{B18}$$

APPENDIX C: SPECTRUM OF A SINGLE MUFFIN-TIN POTENTIAL

Here we discuss the x-ray spectrum for a core state $c=(n,l,J)$ of a single muffin-tin potential confined in a sphere of radius S embedded in a constant potential V_0. The corresponding final states are plane waves scattered by the central potential. For the relativistic case, these can be written in terms of eigenfunctions $|l',J',M'\rangle$ of the total angular momentum $\vec{J}=\vec{L}+\vec{s}$ as

$$\psi_{kl'J'M'}(\vec{r})=\phi_{l'J'}(E,r)\,|\,l',J',M'\rangle\ , \tag{C1}$$

where ϕ_{lJ} is a solution of the Pauli equation with the normalization (2.8). The dispersion relation $E=k^2+V_0$ is determined by the free-electron character of the final states at large distances. The corresponding spectrum $F^{\rm at}_{n,l,J}(E)$ is given by

$$\frac{\omega}{3}F^{\rm at}_{n,l,J}(E)=\int\frac{k^2dk}{2\pi^2}\delta(E-k^2+V_0)\sum_{l',J',M'}\sum_{M}|\langle n,l,J,M\,|\,r\,|\,E,l',J',M'\rangle|^2 \tag{C2}$$

$$=4\pi(2J+1)N^{\rm FE}(E)\sum_{l'}\sum_{J'=l'\pm1/2}(E,l',J'\,|\,r\,|\,n,l,J)^2\Theta(J,J')\ , \tag{C3}$$

where we have again utilized Eq. (13^3.1) of Condon and Shortley[31] as well as (B15). Notice that the atomic spectrum is proportional to the free-electron density of states. Substituting the reduced matrix elements given by (B13), we have

$$\frac{\omega}{3}F^{\rm at}_{n,l,J=l\pm1/2}(E)=\tfrac{1}{4}(2J+1)N^{\rm FE}(E)\left[\frac{2J+3}{J+1}M^2_{l+1,J+1}(E)+\frac{1}{J(J+1)}M^2_{l\pm1,J}(E)+\frac{2J-1}{J}M^2_{l-1,J-1}(E)\right]\ , \tag{C4}$$

where

$$M_{l',J'}(E)=4\pi\int_0^{S_{\rm ws}}r^2\,dr\phi_{nlJ}(r)r\phi_{l'J'}(E,r)\ . \tag{C5}$$

In the limit in which we neglect spin-orbit coupling for the final state, this reduces to

$$\frac{\omega}{3}F^{\rm at}_{n,l,J}(E)=\frac{2J+1}{2(2l+1)}N^{\rm FE}(E)[(l+1)M^2_{l+1}(E)+lM^2_{l-1}(E)]\ . \tag{C6}$$

---

[1]See, for example, L. V. Azaroff and D. M. Pease, in *X-Ray Spectroscopy,* edited by L. V. Azaroff (McGraw-Hill, New York, 1974); L. G. Parrat, Rev. Mod. Phys. 31, 616 (1959); *Soft X-Ray Band Spectra and the Electronic Structure of Metals,* edited by D. J. Fabian (Academic, New York, 1968).

[2]For a review, see P. A. Lee, C. H. Citrin, P. Eisenberger, and B. M. Kinkaid, Rev. Mod. Phys. 53, 769 (1981); T. M. Hayes and J. B. Boyce in *Solid State Physics* edited by H. Ehrenreich, F. Seitz, and D. Turnbull (Academic, New York, 1982), Vol. 37. See also J. E. Müller and W. L. Schaich, Phys. Rev. B 27, 6489 (1983).

[3]P. J. Durham, J. B. Pendry, and C. H. Hodges, Solid State Commun. 38, 159 (1981).

[4]F. Szmulowicz and B. Segall, Phys. Rev. B 21, 5628 (1980).

[5]F. Szmulowicz and D. M. Pease, Phys. Rev. B 17, 3341 (1978).

[6]R. P. Gupta, A. J. Freeman, and J. D. Dow, Phys. Lett. 59A, 226 (1976).

[7]R. P. Gupta and A. J. Freeman, Phys. Lett. 59A, 223 (1976).

[8]R. P. Gupta and A. J. Freeman, Phys. Rev. Lett. 36, 1194 (1976).

[9]J. W. McCaffrey and D. A. Papaconstantopoulos, Solid State Commun. 14, 1055 (1974).

[10]D. J. Negel, D. A. Papaconstantopoulos, J. W. McCaffrey, and J. W. Criss, in *Proceedings of the International Symposium on X-Ray Spectra and Electronic Structure of Matter,* edited by A. Faessler and G. Wiech (Academic, New York, 1973).

[11]D. A. Papaconstantopoulos, Phys. Rev. Lett. 31, 1050 (1973).

[12]S. Wakoh and Y. Kubo, Technical Report of the Institute of Solid State Physics (University of Tokyo), Series A, No. 925 (1978) (unpublished).

[13]J. E. Müller O. Jepsen, O. K. Andersen, and J. W. Wilkins, Phys. Rev. Lett. 40, 720 (1978).

[14]O. K. Andersen, Phys. Rev. B 12, 3060 (1975).

[15]J. E. Müller, O. Jepsen, and J. W. Wilkins, Solid State Commun. 42, 365 (1982).

[16]J. E. Müller, Ph. D. thesis, Cornell University, 1980 (unpublished).

[17]For a discussion of the theory, see G. D. Mahan in *Solid State Physics,* edited by H. Ehrenreich, F. Seitz and D. Turnbull (Academic, New York, 1974), Vol. 29; J. W. Wilkins in *X-Ray*

and Atomic Inner-Shell Physics—1982, edited by B. Crasemann (AIP, New York, 1982). For a discussion of the experimental situation, see C. H. Citrin, G. K. Wertheim, and M. Schlüter, Phys. Rev. B 20, 3067 (1979).

[18]G. Materlik, J. E. Müller, and J. W. Wilkins, Phys. Rev. Lett. 50, 267 (1983).

[19]G. Breit and H. A. Bethe, Phys. Rev. 93, 888 (1954). See also H. A. Bethe and E. E. Salpeter, *Quantum Mechanics of One- and Two-Electron Atoms* (Springer, Berlin, 1957), Secs. 59 and 61.

[20]U. Fano and J. W. Cooper, Rev. Mod. Phys. 40, 441 (1968).

[21]See also L. F. Mattheiss and R. E. Dietz, Phys. Rev. B 22, 1663 (1980).

[22]See, for instance, T. L. Loucks, *Augmented Plane Wave Method: A Guide to Performing Electronic Structure Calculations* (Benjamin, New York, 1967); L. F. Mattheiss, J. H. Wood, and J. C. Switendick, Methods Comput. Phys. 8, 64 (1968).

[23]Early linearization schemes can be found in J. C. Slater, Phys. Rev. 92, 603 (1953); M. M. Saffren and J. C. Slater, *ibid.* 92, 1126 (1953); D. J. Horwarth, *ibid.* 99, 469 (1955).

[24]The same holds for the linear APW method proposed by T. Takeda and J. Kübler, J. Phys. F 9, 661 (1979).

[25]L. F. Mattheiss, Phys. Rev. 133, A1399 (1964).

[26]B. Lengeler (private communication).

[27]O. Jepsen and O. K. Andersen, Solid State Commun. 9, 1963 (1971); G. Lehmann and M. Taut, Phys. Status Solidi 37, K27 (1970).

[28]G. Gilat and L. J. Raubenheimer, Phys. Rev. 144, 390 (1966). See also G. Gilat, Phys. Rev. B 26, 2243 (1982).

[29]Compilations of core-hole widths have been given by K. D. Sevier, *Low-Energy Electron Spectroscopy* (Wiley-Interscience, New York, 1972), Chap. 6; O. Keski-Rahkonen and M. O. Krause, At. Data Nucl. Data Tables 14, 139 (1974).

[30]I. Lindau and W. E. Spicer, J. Electron Spectrosc. 3, 409 (1974); C. J. Powell, Surf. Sci. 44, 29 (1974).

[31]E. U. Condon and G. H. Shortley, *The Theory of Atomic Spectra* (Cambridge University Press, Cambridge, United Kingdom, 1951).